

Fully nonlinear wave-current interactions and kinematics by a BEM-based numerical wave tank

S. Ryu, M. H. Kim, P. J. Lynett

336

Abstract A numerical wave tank (NWT) with fully nonlinear free-surface boundary conditions is developed to investigate nonlinear wave–wave and wave–current interactions and the resulting kinematics. In the present paper, the variation of wave amplitude and wave length of a monochromatic wave under several different speeds of steady uniform currents is studied through direct numerical simulations in the time domain. The nonlinear wave–current interactions are solved using a boundary integral equation method (BIEM) and a Mixed Eulerian–Lagrangian (MEL) time marching scheme. Both a semi-Lagrangian approach and Lagrangian (material-node) approach are employed and their performance is compared. A regridding algorithm based on cubic spline fitting is devised for updating the free-surface moving boundary in a stable and accurate manner. The incident waves are generated by feeding prescribed analytical waves on the input boundary. An efficient artificial numerical beach is devised and applied to dissipate wave energy and minimize wave reflections from the downstream wall. Nonlinear wave kinematics as a result of nonlinear wave–current interactions is calculated and the results are compared with a multi-layer Boussinesq model. The spatial variation of nonlinear wave profiles and kinematics affected by currents are also addressed and discussed.

Keywords Wave-current interaction, Boundary Element Method, Numerical Wave Tank, Multi-layer Boussinesq model, Wave mechanics

1

Introduction

Wave-current interactions have been one of the most interesting, applicable topics in ocean engineering and physical oceanography. For instance, when ocean waves enter an inlet against an ebb current, changes of wave heights and wavelengths occur, which is important to the design or modification of inlet channels for navigation or dredging operations [18]. To solve wave–current interactions, Isaacson and Cheung [10], and Kim and Kim [12] used BEM and perturbation methods for sufficiently small

Froude numbers. On the other hand, Celebi [3] and Celebi et al. [4] investigated transient and steady-state nonlinear wave–current-body interactions by a fully nonlinear 3-D numerical wave tank with a mixed Eulerian–Lagrangian (MEL) time stepping technique. A material node approach was used in their numerical scheme for updating the nonlinear free surface.

Though there are many papers dealing with wave–current interactions based on linear or perturbation theories, for instance the paper of Baddour and Song [1], publications on fully nonlinear wave–current interactions are rare. Furthermore, nonlinear wave–current interactions are very difficult subjects to be studied in the laboratory because it is not easy to generate a uniform steady current field with waves. In this paper, fully nonlinear wave–current interactions, BEM modeling, and the use of a Lagrangian and regridding scheme is addressed. A number of difficulties associated with numerical implementations are discussed. The change of wave amplitudes, shapes, and wave lengths due to coplanar and opposing uniform currents is also discussed. The wave induced particle velocities, particularly the wave kinematics above MWL, are also obtained. The nonlinear solutions are compared with those of linear theory.

Both Lagrangian (material-node) and semi-Lagrangian approaches are independently developed and the results are cross-checked. Several case studies are carried out to check the overall performance of the developed BEM and time-marching scheme. Various interesting features of the fully nonlinear wave–current interactions can be seen through those examples. The simulated results are compared with the results of a multi-layer Boussinesq model, which represents a very different type of model. The two independent numerical models are in excellent agreement both in free-surface profiles and kinematics.

2

Mathematical formulation

It is assumed that the fluid is irrotational and inviscid so that a velocity potential exists in the fluid domain. The domain and coordinate system are shown in Fig. 1. A Cartesian coordinate system is employed such that the $z = 0$ line corresponds to the still water level, z is positive upwards. Now the problem to solve is to determine the velocity potential that satisfies the Laplace equation:

$$\nabla^2 \phi = 0 \quad \text{in } \Omega \quad (1)$$

where Ω denotes the fluid domain.

S. Ryu (✉), M. H. Kim, P. J. Lynett
Coastal and Ocean Engineering Division,
Department of Civil Engineering,
Texas A&M University, College Station,
TX 77843, USA
(e-mail: sryu@tamu.edu)

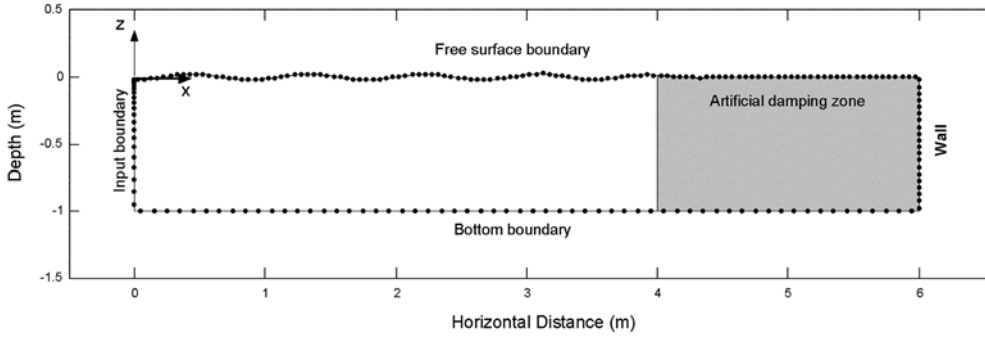


Fig. 1. Schematic diagram of NWT and nodes

Given the boundary conditions, the velocity potential ϕ can be determined by solving the following boundary integral equation:

$$\frac{1}{4\pi} \int_{\Gamma} \left[G(p, q) \frac{\partial \phi(q)}{\partial n(q)} - \phi(q) \frac{\partial G(p, q)}{\partial n(q)} \right] d\Gamma_q = C(p)\phi(p), \quad p \in \Gamma \quad (2)$$

where Γ denotes the boundaries, $G(p, q)$ Green function, $C(p)$ the normalized solid angle at a point on the boundary, and p and q the field and source points, respectively.

2.1 The mixed initial boundary value problem

For 2-D surface wave propagation problems with a steady uniform current parallel to x -direction, the total velocity potential Φ can be expressed as

$$\Phi = U_0 x + \phi(x, z, t) \quad (3)$$

where U_0 is the steady uniform current and $\phi(x, z, t)$ is the unsteady wave potential. Both the total and wave potentials satisfy the Laplace equation. For ϕ , the boundary condition on the right side vertical wall Γ_r is no-flux condition. In mathematical expression, we can write

$$\frac{\partial \Phi}{\partial n} = U_0 + \frac{\partial \phi}{\partial n} = U_0 \quad \text{or} \quad \frac{\partial \phi}{\partial n} = 0 \quad \text{on} \quad \Gamma_r \quad (4)$$

The transmitted and reflected waves inside the damping zone should be completely dissipated. To generate a wave along the input boundary of the NWT, a theoretical fluid particle velocity is applied as a feeding function. The fluid in the wave tank is initially at rest and the incident wave is generated gradually by applying a ramp function to minimize the influence of transient long waves. On the input boundary Γ_w the boundary condition is

$$\frac{\partial \Phi}{\partial n} = -\frac{\partial \phi_w}{\partial x} - U_0 \quad \text{or} \quad \frac{\partial \phi}{\partial n} = -\frac{\partial \phi_w}{\partial x} \quad \text{on} \quad \Gamma_w \quad (5)$$

For the bottom boundary condition, the condition of no flux through the bottom boundary Γ_b gives

$$\frac{\partial \Phi}{\partial n} = \frac{\partial \phi_b}{\partial n} + 0 \quad \text{or} \quad \frac{\partial \phi}{\partial n} = 0 \quad \text{on} \quad \Gamma_b \quad (6)$$

In addition, both the kinematic and dynamic free-surface boundary conditions (FSBCs) must be satisfied on the instantaneous free surface Γ_f . The kinematic FSBC

requires that the free-surface velocity should be equal to the motion of free-surface particles,

$$\frac{D(z - \eta)}{Dt} = 0 \quad \text{on} \quad \Gamma_f \quad (7)$$

$$-\frac{\partial \eta}{\partial t} - \frac{\partial \Phi}{\partial x} \frac{\partial \eta}{\partial x} + \frac{\partial \Phi}{\partial z} = 0 \quad (8)$$

where $z = \eta(x, t)$ is the free-surface elevation. Substituting Eq. (3) into Eq. (8) yields

$$-\frac{\partial \eta}{\partial t} - \left(U_0 + \frac{\partial \phi}{\partial x} \right) \frac{\partial \eta}{\partial x} + \frac{\partial \phi}{\partial z} = 0 \quad (9)$$

$$\frac{\partial \eta}{\partial t} = -\frac{\partial \phi}{\partial x} \frac{\partial \eta}{\partial x} + \frac{\partial \phi}{\partial z} - U_0 \frac{\partial \eta}{\partial x} \quad \text{on} \quad \Gamma_f \quad (10)$$

In addition to the kinematic FSBC Eq. (10), the dynamic FSBC requires that the pressure on the free-surface must be uniform and equal to atmospheric pressure. The Bernoulli equation can be applied to describe this boundary condition,

$$\frac{\partial \Phi}{\partial t} + \frac{1}{2} |\nabla \Phi|^2 + g\eta = -\frac{P_a}{\rho} \quad (11)$$

where the atmospheric pressure P_a can be set to zero and

$$\begin{aligned} |\nabla \Phi|^2 &= \left(\frac{\partial \Phi}{\partial x} \right)^2 + \left(\frac{\partial \Phi}{\partial z} \right)^2 \\ &= \left(\frac{\partial \phi}{\partial x} \right)^2 + \left(\frac{\partial \phi}{\partial z} \right)^2 + 2U_0 \frac{\partial \phi}{\partial x} + U_0^2 \end{aligned} \quad (12)$$

Substituting Eq. (12) into Eq. (11) yields the dynamic FSBC,

$$\frac{\partial \phi}{\partial t} = -g\eta - \frac{1}{2} \left\{ \left(\frac{\partial \phi}{\partial x} \right)^2 + \left(\frac{\partial \phi}{\partial z} \right)^2 \right\} - U_0 \frac{\partial \phi}{\partial x} \quad \text{on} \quad \Gamma_f \quad (13)$$

To solve this boundary value problem in the time domain, initial conditions are required, which can be described as:

$$\phi = 0 \quad (\text{in fluid domain, at } t = 0) \quad (14)$$

$$\eta = 0 \quad (\text{on free surface, at } t = 0) \quad (15)$$

When the nonlinear dynamic and kinematic FSBCs, i.e. Eqs. (10) and (13), are linearized, the corresponding total potential is given by

$$\Phi = U_0 x + \frac{gA \cosh[k(z+h)]}{\omega \cosh kh} \sin(kx - \omega t) \quad (16)$$

where k is wave number, g gravitational acceleration, h water depth, A wave amplitude, and ω circular wave frequency. This formula represents the combined wave and current field, which is independently generated, then the dispersion relation can be written as follows

$$(\omega - kU_0)^2 = kg \tanh kh \quad (17)$$

and the corresponding surface elevation is given by

$$\eta = A \left(1 - \frac{kU_0}{\omega} \right) \cos(kx - \omega t) \quad (18)$$

It can be seen that the wave amplitude increases in opposing current and decreases in coplanar current. On the other hand, wave length is shortened in opposing current and lengthened in coplanar current [6].

2.2

Matrix formulation

In this NWT, the constant elements are employed and the nodes are at the middle of each segment. The discretized formula based on the constant element method of Eq. (2) for a given point 'i' before applying any boundary conditions is as follows [2],

$$\frac{1}{2} u_i + \sum_{j=1}^N \left(\int_{\Gamma_j} q^* d\Gamma \right) u_j = \sum_{j=1}^N \left(\int_{\Gamma_j} u^* d\Gamma \right) q_j \quad (19)$$

Using the symbols \hat{H}_{ij} and G_{ij} for the left and right integrals in the parentheses, we have

$$\frac{1}{2} u_i + \sum_{j=1}^N \hat{H}_{ij} u_j = \sum_{j=1}^N G_{ij} q_j \quad (20)$$

The integrals are calculated by a 4-point Gauss quadrature method and let H_{ij} as follows

$$H_{ij} = \begin{cases} \hat{H}_{ij} & \text{when } i \neq j \\ \hat{H}_{ij} + \frac{1}{2} & \text{when } i = j \end{cases} \quad (21)$$

The entire set of equations can be expressed in matrix form as,

$$\mathbf{H}\mathbf{U} = \mathbf{G}\mathbf{Q} \quad (22)$$

In order to place the unknown and known values of u 's and q 's on the left and right sides, respectively, the rearranged equation can be written as

$$\tilde{\mathbf{H}} \begin{Bmatrix} \phi_w \\ \phi_b \\ \phi_r \\ (\phi_f)_n \end{Bmatrix} = \tilde{\mathbf{G}} \begin{Bmatrix} (\phi_w)_n \\ (\phi_b)_n \\ (\phi_r)_n \\ \phi_f \end{Bmatrix} \quad (23)$$

where matrices $\tilde{\mathbf{H}}$ and $\tilde{\mathbf{G}}$ are the rearranged matrices by switching last m columns between \mathbf{H} and \mathbf{G} , where m is the total number of nodes on the free-surface, ϕ_w , ϕ_b , ϕ_r , and ϕ_f the potentials on the wavemaker, bottom, right-hand

side wall, and free surface, respectively, as shown in the Fig. 1. The subscript n represents the normal derivative and the corresponding initial input boundary conditions were given in Sect. 3.1. Note that if the potential on the wavemaker boundary is used, ϕ_w and $(\phi_w)_n$ and the corresponding columns of \mathbf{H} and \mathbf{G} should be switched. However, $(\phi_w)_n$ resembling ideal flexible wavemaker was chosen as the input incident wave potential for the NWT in this study. Finally, we can pass all unknowns to the left-hand side and write,

$$\mathbf{X} = \mathbf{A}^{-1}\mathbf{F} \quad (24)$$

where \mathbf{X} is the vector of unknown u 's and q 's, $\mathbf{A}^{-1} = \tilde{\mathbf{H}}^{-1}\tilde{\mathbf{G}}$, and \mathbf{F} the vector of known u 's and q 's.

2.3

FSBCs by Lagrangian or semi-Lagrangian approach

If a Lagrangian approach is applied, the kinematic and dynamic FSBCs must be described based on the total derivative. Then, Eqs. (10) and (13) can be changed to the following forms, respectively,

$$\frac{\delta \eta}{\delta t} = -(\nabla \phi - \vec{v}) \cdot \nabla \eta + \frac{\partial \phi}{\partial z} - U_0 \frac{\partial \eta}{\partial x} \quad \text{on } \Gamma_f \quad (25)$$

and

$$\begin{aligned} \frac{\delta \phi}{\delta t} = & -g\eta - \frac{1}{2} \left\{ \left(\frac{\partial \phi}{\partial x} \right)^2 + \left(\frac{\partial \phi}{\partial z} \right)^2 \right\} \\ & + \vec{v} \cdot \nabla \phi - U_0 \frac{\partial \phi}{\partial x} \quad \text{on } \Gamma_f \end{aligned} \quad (26)$$

where \vec{v} is the node velocity and the total derivative

$$\frac{\delta}{\delta t} \equiv \frac{\partial}{\partial t} + \vec{v} \cdot \nabla \quad (27)$$

If the nodal velocity \vec{v} is moving with time but chosen other than the fluid particle velocity, it is called semi-Lagrangian approach. When a semi-Lagrangian approach is applied in this paper, the node is restricted to move vertically following the free surface.

In this paper, a material-node approach is employed so that every individual free-surface node or collocation point should follow the corresponding individual fluid particles, i.e. $\vec{v} = \nabla \Phi$ [3]. Then the position vector of a fluid particle on the free-surface $\vec{X}_f(t) = \{x_f(t), z_f(t)\}$ and its material derivative are given by

$$\frac{\delta \vec{X}_f(t)}{\delta t} = \vec{v}(\vec{x}, t) = U_0 \vec{i} + \nabla \phi \quad (28)$$

Applying Eq. (28) into the FSBCs, Eqs. (25) and (26) yield

$$\frac{\Delta \eta}{\Delta t} = \frac{\partial \phi}{\partial z} \quad \text{on } \Gamma_f \quad (29)$$

and

$$\frac{\Delta \phi}{\Delta t} = -g\eta + \frac{1}{2} \left\{ \left(\frac{\partial \phi}{\partial x} \right)^2 + \left(\frac{\partial \phi}{\partial z} \right)^2 \right\} \quad \text{on } \Gamma_f \quad (30)$$

The material-node Eqs. (29) and (30) become simpler compared to the semi-Lagrangian Eqs. (25) and (26).

3 Numerical schemes

3.1 Artificial damping and time marching

At the end of the NWT, an artificial damping zone is established with extra damping terms on both kinematic and dynamic free-surface conditions. The effectiveness of such damping terms is well demonstrated in [13]. Both leapfrog scheme (LF) and 4th-order Runge-Kutta scheme (RK4) were used for cross-checking the time marching of free-surface. For spatial derivatives $\partial\eta/\partial x$ and $\partial\phi_f/\partial x$, both central differencing and analytic differentiation of cubic spline functions were applied for double checking.

For instance, the difference forms of Eqs. (10) and (13) based on a semi-Lagrangian approach and the LF in the artificial damping zone can be written as follows

$$\eta^{k+\frac{1}{2}} = \eta^k + \Delta t \left(\frac{\partial\phi_f^k}{\partial z} - \frac{\partial\phi_f^k}{\partial x} \frac{\partial\eta^k}{\partial x} + U_0 \frac{\partial\eta^k}{\partial x} - \mu_2 \eta^k \right) \quad (31)$$

$$\phi_f^{k+1} = \phi_f^k + \Delta t \left(-g\eta^{k+\frac{1}{2}} + \frac{1}{2} |\nabla\phi_f^k|^2 + U_0 \frac{\partial\phi_f^k}{\partial x} - \mu_1 \frac{\partial\phi_f^k}{\partial z} \right) \quad (32)$$

where ϕ_f is the free-surface unsteady potential and μ_1 and μ_2 are damping coefficients for the artificial numerical beach as shown in Fig. 1. Here, if two damping coefficients are set to zero, then the above two equations become ordinary FSBCs without any artificial damping.

If a material-node approach is used, Eqs. (31) and (32) can be rewritten as follows

$$\eta^{k+\frac{1}{2}} = \eta^k + \Delta t \left(\frac{\partial\phi_f^k}{\partial z} - \mu_2 \eta^k \right) \quad (33)$$

$$\phi_f^{k+1} = \phi_f^k + \Delta t \left(-g\eta^{k+\frac{1}{2}} + \frac{1}{2} |\nabla\phi_f^k|^2 - \mu_1 \frac{\partial\phi_f^k}{\partial z} \right) \quad (34)$$

One of the advantages in the use of Eqs. (33) and (34) is that there is no convection-like term in the difference equations, so the numerical implementation is much simpler. When a semi-Lagrangian approach was used with current, $U_0\partial\eta/\partial x$ and $U_0\partial\phi/\partial x$ act like damping in x -direction, and thus special care should be taken to remove such phenomena. Therefore, in the case of nonlinear free-surface simulations with current, the material-node approach is more robust and effective.

3.2 Tracking Lagrangian points

At every time step, the updated location of each point can be traced by the following formulas:

$$x^{k+1} = x^k + \Delta t \left(U_0 + \frac{\partial\phi_f^k}{\partial x} \right) \quad (35)$$

$$z^{k+1} = \eta^{k+1} \quad (36)$$

3.3 Special numerical treatments at free-surface/wavemaker intersection

To generate a wave in this NWT, numerical velocity input on inflow boundary is applied as a feeding function. The fluid in the wave tank is initially at rest and the incident wave is generated gradually by applying a ramp function to avoid impulsive motion of the first waves.

When the Lagrangian approach is used, it is noted that the first collocation point x_1 on the free-surface close to the left vertical boundary Γ_w can cause a numerical instability problem. Especially, the x -location of the first collocation point in a coplanar current case could be much greater than the location of the original position. In that case, if an extrapolation method is applied to get the updated values of η and ϕ_f as part of regridding procedure, the extrapolated values may not be accurate. To resolve this problem, the following logical statement was applied in a computer program.

If $x_1 > \frac{\Delta x}{2}$, where Δx is the size of uniform grid on the free-surface boundary, the analytic expressions of the feeding η and ϕ_w were used at $x = 0$ and the corresponding values at x_1 were interpolated.

4 Grid generation

4.1 Grid spacing on the input boundary

To investigate the accuracy and efficiency depending on the total number of nodal points and the nodal spacing at the vertical boundaries, three mathematical functions are considered. They are: (1) uniform spacing, (2) hyperbolic cosine function, and (3) inverse sine function.

Based on several simulations with different spacing algorithms described above, it is shown that the input boundary spacing obtained from a hyperbolic cosine function is superior to other spacing techniques. The efficiency of the grid spacing can be verified by comparing those simulation results to a higher order nonlinear wave theory, for instance 2nd order Stokes waves. In addition, it is certain that a much finer grid system based on a hyperbolic function, which is a base function of linear gravity waves, can represent the rapid change of the potential values as z gets closer to the free surface.

It may not be easy to directly feed the inflow uniform current at the input boundary because the length of the vertical boundary changes with fluctuating free surface. Therefore, the current field is separated from the unsteady potential and directly applied to the entire field.

4.2 Regridding

At every time step, in order to keep the original free-surface grid spacing, a cubic spline function is applied for interpolation along the free surface. To calculate the spatial derivative in Eq. (34) with respect to the variable x , the analytic derivative of the piecewise cubic functions is applied. The analytic derivative was confirmed by comparing with central difference scheme.

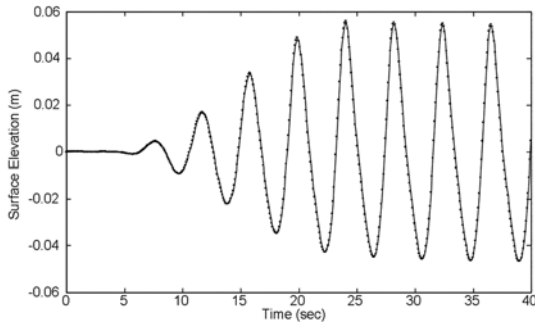


Fig. 2. Comparison of results obtained from a Lagrangian grid plus regridding (dots) and a semi-Lagrangian grid (solid line). Linear input values are: wave amplitude $A = 0.05$ m, wave period $T = 4.17$ s, wavelength $L = 12.57$ m, and water depth $h = 1$ m (intermediate water)

4.3

Consideration of grid spacing and time increment

In numerical calculations, grid spacing Δx and time increment Δt must be chosen to avoid numerical instability and to achieve desirable accuracy. Dommermuth and Yue [7] performed a Von Neumann stability analysis for RK4, with linearized free-surface conditions, and obtained the following Courant condition

$$\Delta t^2 \leq \frac{8 \Delta x}{\pi g} \quad (37)$$

where Δt is the time step, and Δx the local grid spacing. Although Eq. (37) is a required numerical stability condition for linearized free-surface conditions, we expect

that it should at least be satisfied for nonlinear problems as well [11]. The regridding was done at every time step. The regridding technique includes cubic spline interpolation, and thus additional smoothing is not necessary.

4.4

Lagrangian vs. semi-Lagrangian methods

First, the free-surface simulations without current were carried out by using both Lagrangian and semi-Lagrangian approach for cross-checking. In the semi-Lagrangian approach, the node is forced to move vertically, and thus regridding is not necessary. It is confirmed as in Fig. 2 that both methods produce almost the same results. It can also be noted that the intermediate water waves in Fig. 2 have nonlinear wave features, i.e. narrower and higher crests and shallower and wider troughs. The performance of the present scheme for artificial damping zone appears to be excellent minimizing wave reflection into the wave field.

5

Case study

Several cases are addressed in this section to better understand the phenomena of nonlinear wave-current interactions. First, it is observed as expected that nonlinear phenomena, such as crest-trough asymmetry, skewness, secondary peaks etc. are more pronounced when water depth is shallower and the wave steepness becomes greater. Secondly, changes of crests, troughs, and wavelength as a function of current speed are quantitatively shown. Finally, practical problems that may be difficult to solve theoretically or by experiments, such as nonlinear

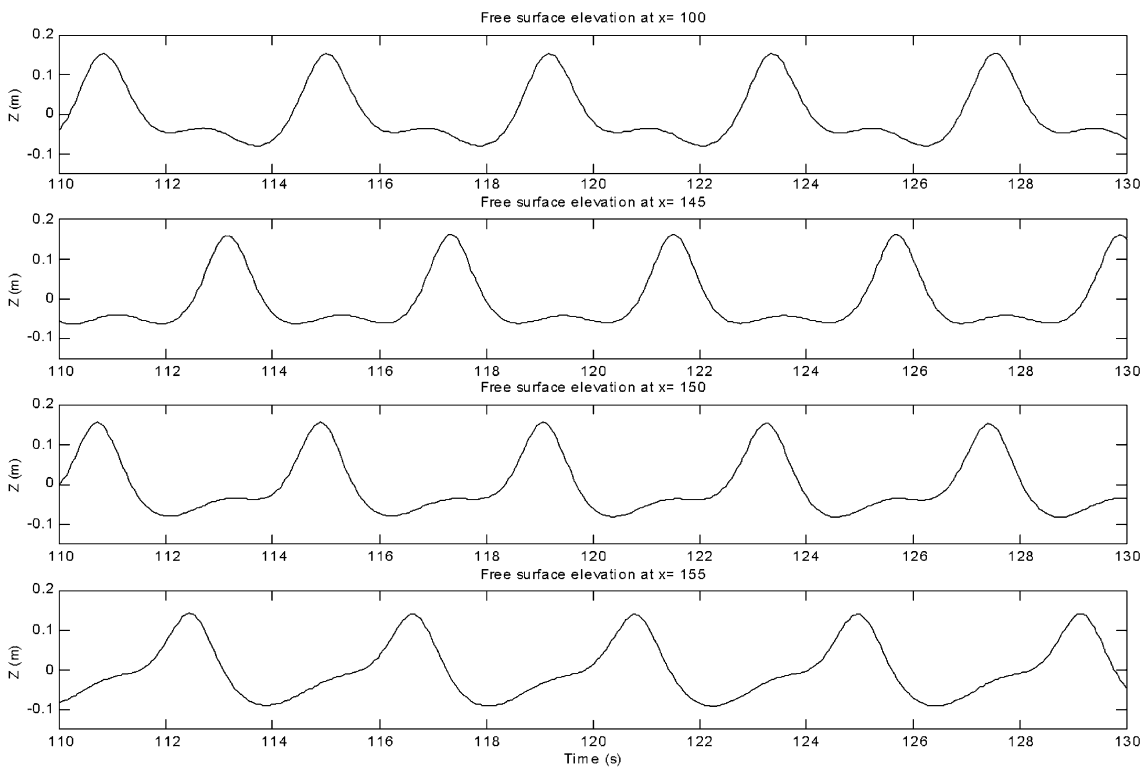


Fig. 3. Long range traveling waves show the spatial change of free surface elevations recorded at $x = 100, 145, 150,$ and 155 m from the wavemaker, respectively

wave–current kinematics above mean water level, are simulated based on the developed NWT.

5.1

Linear wave input with fully nonlinear FSBCs

The free surface elevation is a function of the input wave feeding function (or wavemaker motion). The cases examined in this paper are in intermediate water depth with:

$$\frac{H}{gT^2} = 0.0006 \sim 0.0012 \quad \text{and} \quad \frac{d}{gT^2} = 0.0059 .$$

Figure 3 shows that when waves are generated in the NWT, spatial variation of the waveform persists even at large distances from the wavemaker unless fully nonlinear kinematics are fed. The spatial variation is more pronounced when the mismatch between the fully nonlinear and linear wave kinematics are larger at the wavemaker boundary.

According to the wave-theory-selection diagram presented by Le Mehaute [14], the cases examined here are near overlapped region among several different wave theories. Cnoidal theory may be a proper choice. The expression for cnoidal waves is based on KdV-type equations, which do not have good nonlinear dispersive properties much past $kh = 0.1$. Therefore, even if cnoidal waveform, which is based on the incorrect (or approximate) physics of the problem, is generated in the NWT, it may be similar to the original problem of putting a linear wave into a nonlinear domain. Additionally, the cnoidal wave is a *weakly nonlinear* wave solution, and will not satisfy the fully nonlinear, fully dispersive equations. Therefore, it may be very difficult to put the “correct” nonlinear wave into the input boundary. Only if an analytic fully-nonlinear wave solution is inputted through the wavemaker will a symmetric nonlinear wave result. A complete nonlinear wave solution for this wave height and period does not exist in a practically-useful, closed form. Hence, the linear wave input with fully nonlinear FSBCs, as in the present case, produces asymmetric and spatially varying waves. The common weakly nonlinear waves, such as stream-function waves [5], cnoidal waves, and high-order Stokes waves, which are symmetric locked waves and do not include nonlinear free waves, may only slightly improve the situation.

Due to a mismatch between the input wavemaker motion and the actual kinematics of fully nonlinear waves, which happens both in physical and numerical wave tanks, the phenomenon of “recurring spatial variation of water waves” occurs [9]. The mismatch at the wave-maker boundary generates a series of high-order free waves traveling at different speeds compared to the primary wave crest, which causes the secondary peaks, asymmetry and distortion, and spatial variation in wave profiles. Therefore, the symmetry with respect to the crest is not likely to be achieved unless the effects of free waves are negligible (or perfectly fully-nonlinear wave kinematics are fed).

The free waves continue to propagate further downstream, and thus the simulation does not produce a perfectly symmetric waveform with respect to the crest. Fig. 3 supports the above explanation. Goda conducted experiments in a physical wave tank and explained the phenomenon of

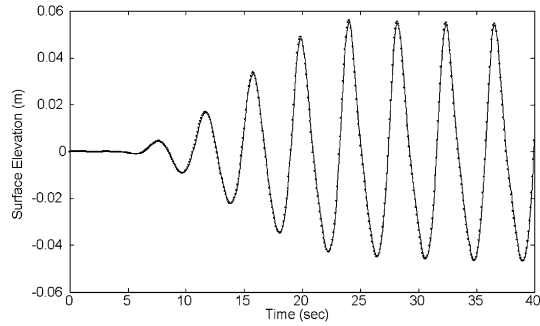


Fig. 4. Convergence test based on wave elevation: Wave elevation comparison with the coarser mesh (solid line) and the finer mesh system (dots) makes 0.77% difference in wave height for 50% increase of the total number of the collocation points

Table 1. Input parameters of two case runs (linear wave)

| Case | A (m) | L (m) | H/L | T (s) | h (m) | k (m ⁻¹) | U ₀ (m/s) |
|------|-------|-------|-------|-------|-------|----------------------|----------------------|
| A | 0.05 | 12.57 | 0.008 | 4.17 | 1.0 | 0.50 | 0.0 |
| B | 0.10 | 12.57 | 0.016 | 4.17 | 1.0 | 0.50 | 0.0 |

the spatial variation of water waves in a laboratory flume [9]. Physical and numerical wave tanks share the similar problem of mismatch at the wavemaker boundary. Hence, spatially varying wave elevations occur in the following cases.

5.2

Convergence test

To conduct a convergence test, the following case was chosen: linear input wave height 5 cm, wave length 12.57 m, the probe located at $x = 10$ m from the left input boundary, total wave tank 50 m including the 20 m-long damping zone. The comparison of the wave elevation time series by applying two different free-surface mesh resolutions is shown in Fig. 4. The coarser grid system has 20 collocation points per wave length and the finer has 50% more points on the free surface i.e. 30 points per wavelength. The difference is less than 0.77%, which leads to a conclusion that this mesh generation is fine enough for this problem. For the rest of the examples presented in this paper, 25 collocation points per wave length were used on the free surface. For the kinematics calculation of the most nonlinear case (Fig. 12), denser grid system (30 points per wavelength) was used to be conservative.

5.3

Nonlinear vs. linear numerical solutions

The wave steepness H/L , which is a ratio of wave height to wavelength, can be an index of nonlinearity of gravity waves. Please note that all numeric values of A , H , and L in the captions of the following figures are linear wave input values. Two different waves were used to investigate how this index affects the wave profiles and wave kinematics. The input values of two simulations are summarized in Table 1. In this example intermediate water depth was chosen.

As the wave steepness increases, nonlinear wave profiles have more skewed non-symmetric forms and the height of wave crests increases and the trough decreases, as shown

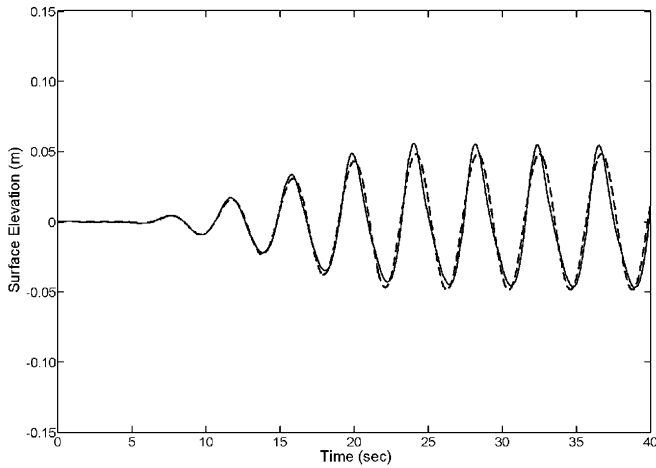


Fig. 5. Case A – Comparison of nonlinear (solid line) and linear (dashes) numerical solutions of $H/L = 0.008$ at $x = 10$ m

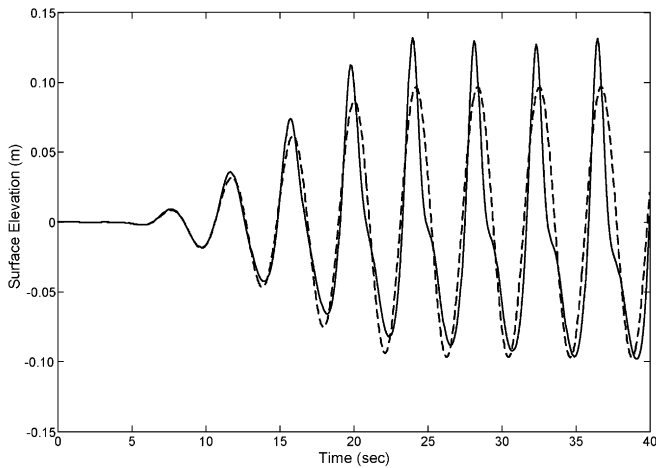


Fig. 6. Case B – Comparison of nonlinear (solid line) and linear (dashes) numerical solutions of $H/L = 0.016$ at $x = 10$ m

in Figs. 5 and 6. Both simulation results show the non-zero mean due to nonlinearity. The overall shape of the waves is shifted upwards. The difference between linear and nonlinear simulation is more pronounced when the wave velocity or acceleration are calculated.

5.4 Multi-layer Boussinesq model

The past decade saw the advent and wide spread applications of Boussinesq-type equation models for studying water wave propagation in one- and two-horizontal dimensions. This depth-integrated modeling approach employs a polynomial approximation of the vertical profile of the velocity field, thereby reducing the dimensions of a three-dimensional problem by one. With the use of an arbitrary vertical evaluation level of the characteristic horizontal velocity vector, the Boussinesq equations have good linear dispersion accuracy to $kh \sim 3$ [17].

Further enhancing the deep-water accuracy of the depth-integrated approach is the so-called high-order Boussinesq-type equations. While the Boussinesq models

Table 2. Input parameters of six cases (incident linear wave condition)

| Case | A (m) | L (m) | H/L | U_0 (m/s) | T (s) | h (m) |
|------|---------|---------|-------|-------------|---------|---------|
| A | 0.05 | 12.57 | 0.008 | 0.313 | 4.17 | 1.0 |
| B | 0.05 | 12.57 | 0.008 | 0.000 | 4.17 | 1.0 |
| C | 0.05 | 12.57 | 0.008 | -0.313 | 4.17 | 1.0 |
| D | 0.10 | 12.57 | 0.016 | 0.313 | 4.17 | 1.0 |
| E | 0.10 | 12.57 | 0.016 | 0.000 | 4.17 | 1.0 |
| F | 0.10 | 12.57 | 0.016 | -0.313 | 4.17 | 1.0 |

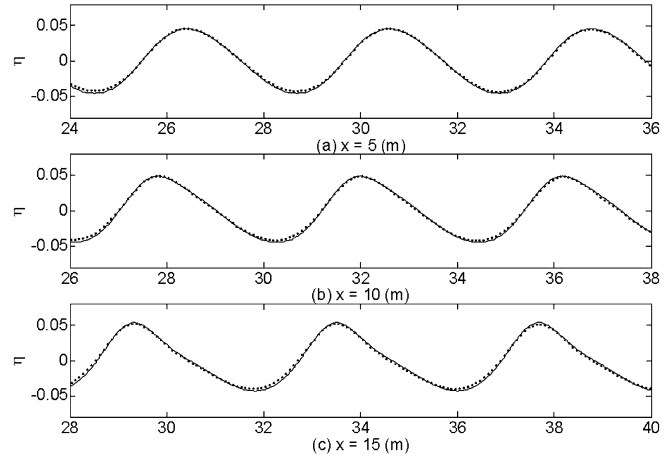


Fig. 7. Time series of nonlinear free-surface wave with coplanar current for the change of wave height. Each probe is located at $x = 5, 10,$ and 15 m, respectively. Input linear wave amplitude is 5 cm

such as Nwogu's use a quadratic polynomial approximation for the vertical flow distribution, these high-order models use fourth, and higher, order polynomial approximations. Gobbi et al. [8], using a fourth-order polynomial, developed a model with excellent linear dispersive properties up to $kh \sim 6$. The multi-layer model employed here represents a different approach to developing a depth-integrated model with high-order dispersive properties.

The multi-layer derivation consists of a piecewise integration of the primitive equations of motion through N constant-density layers of arbitrary thickness. Within each layer, an independent velocity profile is determined. With N separate velocity profiles, matched at the interfaces of the layers, the resulting set of equations have $N + 1$ free parameters, allowing for an optimization with known analytical properties of water waves. The optimized two-layer model equations show good linear wave characteristics up to $kh \sim 8$, while the second-order nonlinear behavior is well captured to $kh \sim 6$. The two-layer model is used for all the results presented in this paper.

A finite difference numerical model is developed for the multi-layer equations, and comparisons with analytical solutions and experimental datasets shows excellent agreement [15, 16]. Waves are generated inside the numerical domain using an internal source generator. The pre-specified current is sent in through the boundaries, and the domain is set large enough such that the internally generated waves do not interact with the lateral boundaries.

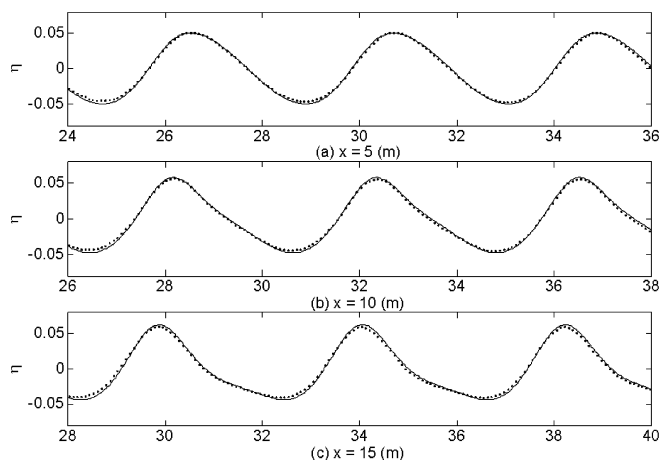


Fig. 8. Time series of nonlinear free-surface wave without current for the change of wave height. Each probe is located at $x = 5, 10,$ and 15 m, respectively. Input linear wave amplitude is 5 cm

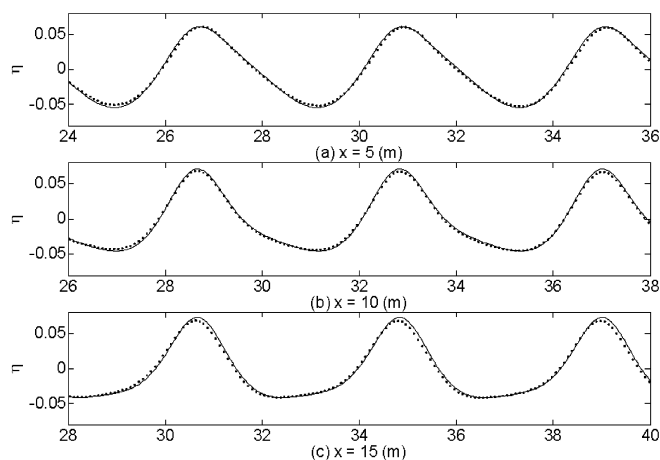


Fig. 9. Time series of nonlinear free-surface wave with opposing current for the change of wave height. Each probe is located at $x = 5, 10,$ and 15 m, respectively. Input linear wave amplitude is 5 cm

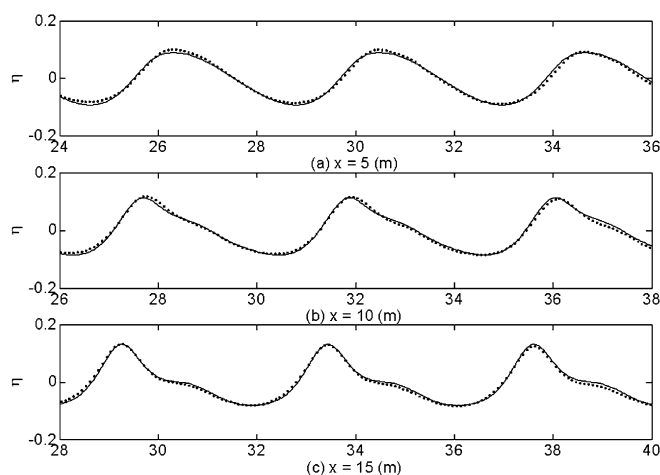


Fig. 10. Time series of nonlinear free-surface wave with coplanar current for the change of wave height. Each probe is located at $x = 5, 10,$ and 15 m, respectively. Input linear amplitude is 10 cm

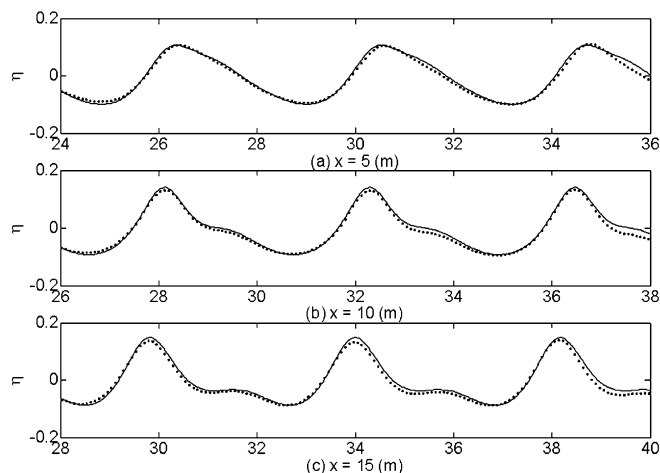


Fig. 11. Time series of nonlinear free-surface wave without current for the change of wave height. Each probe is located at $x = 5, 10,$ and 15 m, respectively. Input linear amplitude is 10 cm

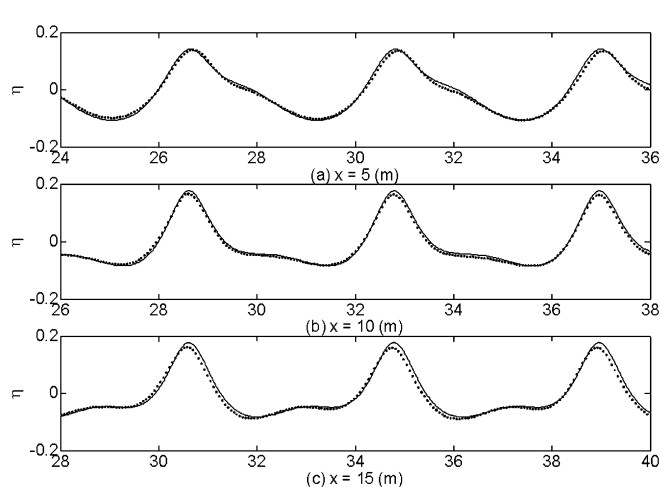


Fig. 12. Time series of nonlinear free-surface wave with opposing current for the change of wave height. Each probe is located at $x = 5, 10,$ and 15 m, respectively. Input linear amplitude is 10 cm

5.5

Comparison with multi-layer Boussinesq model

To investigate the effect of uniform current on nonlinear propagating waves, six different cases are studied. The input values are summarized in Table 2.

As shown in Figs. 7 through 12, the coplanar current following the waves ($U_0 > 0$) makes the wave amplitude smaller, while the opposing current ($U_0 < 0$) amplifies the wave amplitude. This trend can also be seen in linear theory, as predicted by Eq. (18). The figures show the comparison of fully nonlinear simulations obtained from the BEM-based NWT (dots) with ones from the multi-layer Boussinesq model (solid lines). The overall comparison is excellent and confirms the accuracy of the two independent approaches.

When waves interact with opposing currents, stronger nonlinearity appears, which is characterized by a higher and sharper crest, shallower and flatter trough, skewness and asymmetry, and appearance of a secondary peak.

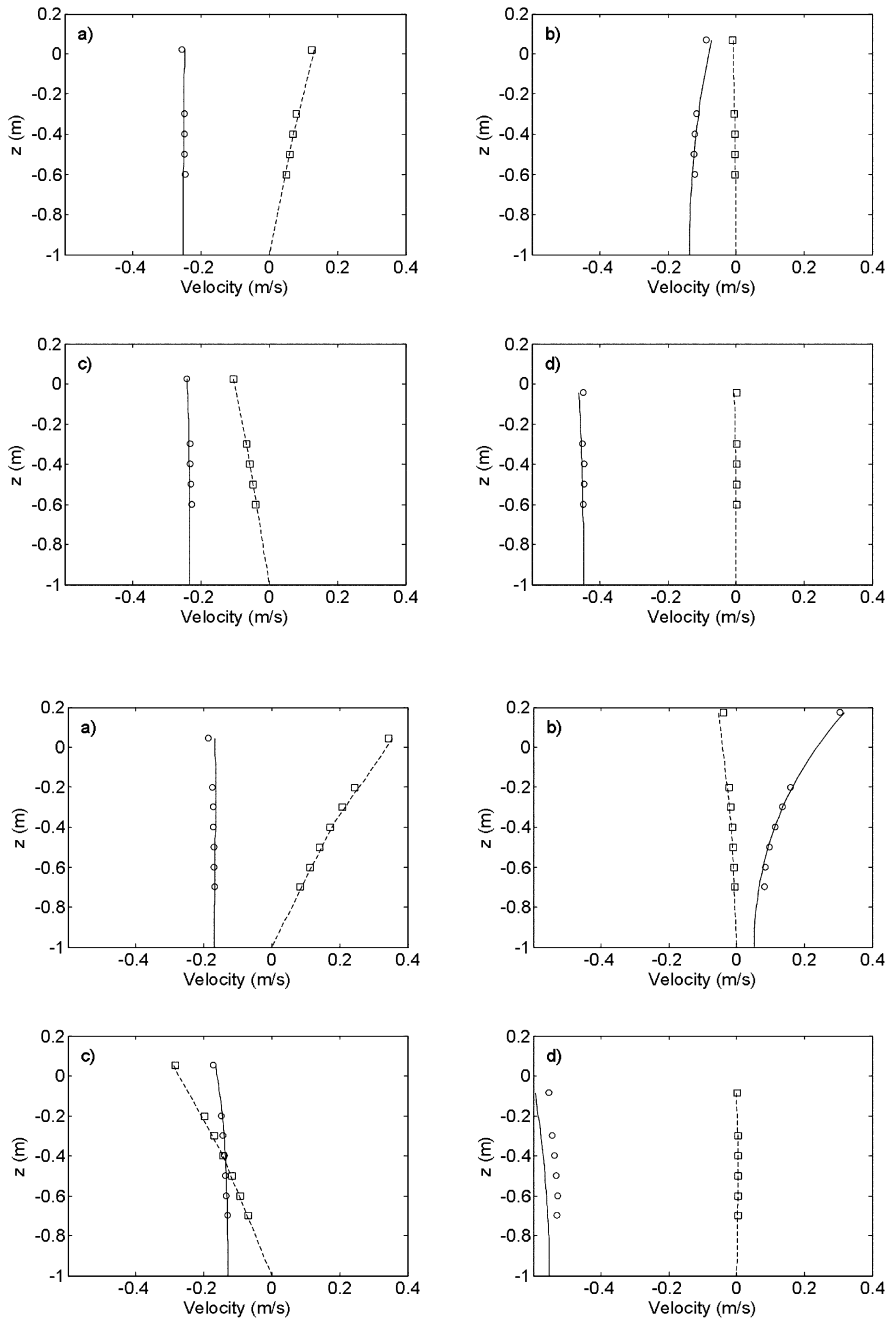


Fig. 13. Vertical profiles of velocity components for $A = 5$ cm (linear wave input), opposing current. The profiles of horizontal velocity (solid line) and the vertical velocity (dashed line) predicted by the Boussinesq-type model. The profiles of the horizontal velocity (circles) and the vertical velocity (squares) predicted by the BEM model. Subplot **a** gives the profiles at the time of maximum vertical velocity, **b** at maximum horizontal velocity (under crest), **c** at minimum vertical velocity, and **d** at minimum horizontal velocity (under trough)

Fig. 14. Vertical profiles of velocity components for $A = 10$ cm (linear wave input), opposing current (Same caption as in Fig. 13)

Figs. 7 through 12 show that the nonlinear features are greatly magnified with increasing incident wave amplitude. It is also found that wave elevation and shape are functions of the horizontal spatial variable x as the waves propagate. It is interesting to see that the wave shape changes appreciably even within a distance of wavelength. In the severest nonlinear case (Fig. 12), we can see the secondary peak propagating at different speed compared to primary wave, which is also demonstrated in [13]. In Figs. 13, 14, and 15, the corresponding wave kinematics results are presented. For the wave kinematics comparison, opposing current cases C and F are selected. It can be concluded that the two totally different numerical models produce almost the same results. In particular, both numerical models produce reliable results for particle velocities above mean water level,

which are difficult to obtain from experiment. Fig. 15 shows time histories of horizontal and vertical particle velocities on the free surface. Both BEM and Boussinesq models show severe nonlinearity, especially in vertical velocities. In the same figure, the range of linear solution is also indicated. Judging from Fig. 15 and Table 3, the difference between linear and nonlinear solutions is much more pronounced in kinematics comparison than in surface-profile comparison. For example, the crest of nonlinear computation can be about twice bigger than that of linear theory, which is also confirmed by the multi-layer Boussinesq model and demonstrates the importance of nonlinear computation.

The comparisons between linear and nonlinear computation for coplanar, no, and opposing current cases are summarized in Table 3. The difference in wavelength

Table 3. Summary of simulation results for the case $A = 10$ cm (linear wave input) on free surface. The crest and trough particle velocities in linear theory are calculated at $z = 0$

| | Coplanar current ($U_o = 0.313$ m/s) | | No current ($U_o = 0$ m/s) | | Opposing current ($U_o = -0.313$ m/s) | |
|----------------------|--|-----------|--------------------------------|-----------|---|-----------|
| | Linear | Nonlinear | Linear | Nonlinear | Linear | Nonlinear |
| Profile(m) | | | | | | |
| Crest | 0.091 | 0.111 | 0.100 | 0.129 | 0.112 | 0.171 |
| Trough | -0.091 | -0.084 | -0.100 | -0.095 | -0.112 | -0.081 |
| Mean | 0 | -0.007 | 0 | -0.013 | 0 | -0.008 |
| Kinematics u (m/s) | | | | | | |
| Crest | 0.606 | 0.721 | 0.326 | 0.491 | 0.055 | 0.346 |
| Trough | 0.020 | 0.071 | -0.326 | -0.261 | -0.681 | -0.557 |
| Mean | 0.313 | 0.325 | 0.000 | -0.001 | -0.313 | -0.316 |
| Kinematics w (m/s) | | | | | | |
| Crest | 0.124 | 0.205 | 0.150 | 0.250 | 0.188 | 0.369 |
| Trough | -0.124 | -0.118 | -0.150 | -0.205 | -0.188 | -0.323 |
| Mean | 0 | 0.000 | 0 | 0.001 | 0 | 0.001 |
| Wavelength (m) | 13.96 | 13.74 | 12.57 | 12.12 | 11.13 | 11.51 |

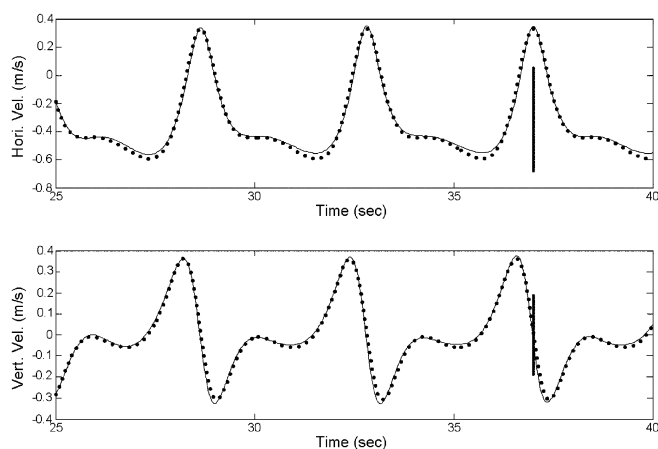


Fig. 15. Comparison of horizontal/vertical velocities at $x = 10$ m on free surface. BEM NWT (solid line), Boussinesq-type model (dots), and the vertical straight lines represent the range of linear solution

between linear and nonlinear solutions is less pronounced compared to crest and trough values.

6 Concluding remarks

In this paper, fully nonlinear wave interactions with steady uniform currents and the resulting kinematics are studied. First, both Lagrangian and semi-Lagrangian schemes are developed. It is shown that the two independent methods produce identical results. The Lagrangian approach is found to be more effective in wave-current simulations. However, the Lagrangian approach requires a regridding scheme to prevent numerical instability. Changes of wave crests, troughs, and wavelength due to wave-current interactions are simulated and compared with the results of a multi-layer Boussinesq numerical model. The nonlinear simulations give, in general, larger and sharper crest amplitudes and velocities compared with linear theory.

For opposing current cases, the wave steepness becomes larger (the crest becomes higher and sharper while the

trough becomes shallower and flatter), as the current speed increases. As a result, both surface profiles and wave kinematics exhibit highly nonlinear features including secondary peaks. For coplanar current cases, the wave amplitudes decrease and the wave length becomes longer as the current speed increases. The nonlinear waves also change shapes even within a couple of wave-length distance as they propagate downstream. More nonlinear features can be observed in farther downstream.

Lastly, wave-current interaction is an important process in various mass transport problems. It can also appreciably increase wave crest height and cause large wave forces when the wave crests run up or hit any part of ocean structures. It is also shown that the crest values in kinematics can be significantly amplified compared with the linear solutions as a result of nonlinear interactions. The observed nonlinear effects may be of significant importance to various environmental problems and the design of coastal and offshore structures.

References

1. Baddour RE, Song S (1990) On the interaction between waves and currents. *Ocean Eng.* 17: 1-21
2. Brebbia CA, Walker S (1980) *Boundary element techniques in engineering*. Newnes-Butterworths
3. Celebi MS (2001) Nonlinear transient wave-body interactions in steady uniform currents. *Comput. Meth. Appl. Mech. Eng.* 190: 5149-5172
4. Celebi MS, Kim MH, Beck RF (1998) Fully nonlinear 3-D numerical wave tank simulation. *J. Ship Res.* 42(1): 33-45
5. Dean RG (1965) Stream function representation of nonlinear ocean waves. *J. Geophysical Res.* 70(18): 4561-4572
6. Dean RG, Dalrymple RA (1991) *Water wave mechanics for engineers and scientists*. World Scientific Publishing Co., pp. 66-69
7. Dommermuth DG, Yue DKP (1987) Numerical simulation of nonlinear axisymmetric flows with a free surface. *J. Fluid Mech.* 178: 195-219
8. Gobbi MF, Kirby JT, Wei G (2000) A fully nonlinear Boussinesq model for surface waves. Part II. Extension to $O(kh)^4$. *J. Fluid Mech.* 405: 182-210
9. Goda Y (1998) Perturbation analysis of nonlinear wave interactions in relatively shallow water. In: Kim H, Lee SH, Lee SJ (Eds), *Intl. Conf. Hydrodynamics*, pp. 33-51

10. **Isaacson M, Cheung KF** (1993) Time-domain solution for wave-current interactions with a two-dimensional body. *Applied Ocean Res.* 15: 39–52
11. **Kim CH, Clement AH, Tanizawa K** (1999) Recent research and development of numerical wave tanks: A Review. *Int. J. Offshore and Polar Eng.*, ISOPE, 9: 241–256
12. **Kim DJ, Kim MH** (1997) Wave-current-body interaction by a time-domain high-order boundary element method. *Proc 7th Int Offshore and Polar Eng Conf, Honolulu, ISOPE, Vol. 3:* 107–115
13. **Koo W, Kim MH** (2001) Fully nonlinear waves and their kinematics: NWT simulation vs. experiment, *Ocean Wave Measurement and analysis. Proc 4th International Symposium WAVES 2001, ASCE, Vol. 2, pp.* 1092–1101
14. **Le Mehaute B** (1969) An introduction to hydrodynamics and water waves, *Water Wave Theories, Vol. II, TR ERL 118-POL-3-2, U.S. Department of Commerce, ESSA, Washington, DC*
15. **Lynett P** (2002) A multi-layer approach to modeling generation, propagation, and interaction of water waves, Ph.D. Thesis, Cornell University
16. **Lynett P, Liu P** (2003) A multi-layer approach to water wave modeling. In review for *Proc. Royal Soc. London A*
17. **Nwogu O** (1993) Alternative form of Boussinesq equations for nearshore wave propagation. *J Waterway, Port, Coastal and Ocean Eng.* 119(6): 618–638
18. **Smith JM** (1997) One-dimensional wave-current interaction. *Coastal Engineering Technical Note, CETN IV-9*